

Pressure-Induced Metal-Insulator Transition in Twisted Bilayer Graphene

Bikash Padhi* and Philip W. Phillips†

*Department of Physics and Institute for Condensed Matter Theory,
University of Illinois at Urbana–Champaign,
1110 West Green Street, Urbana, Illinois 61801, United States*

Abstract

Recent experiments [arXiv:1808.07865] on twisted bilayer graphene (TBLG) show that under hydrostatic pressure, an insulating state at quarter-filling of the moiré superlattice (i.e., one charge per supercell) emerges, in sharp contrast with the previous ambient pressure measurements of Cao *et al.* where the quarter-filling state (QFS) is a metal [Nature 556, 43 & 80 (2018)]. In fact, the insulating state at the other commensurate fillings of two and three charges per supercell is also enhanced under applied pressure. Based on realistic computations of the band structure for TBLG which show that the bandwidth first shrinks and then expands with increasing hydrostatic pressure, we compute the ratio of the potential to the kinetic energy, r_s . We find an experimentally relevant window of pressure for which r_s crosses the threshold for a triangular Wigner crystal, thereby corroborating our previous work [Nano Lett. (2018)] that the insulating states in TBLG are due to Wigner rather than Mott physics. A key prediction of this work is that the window for the onset of the hierarchy of Wigner states that obtains at commensurate fillings is dome-shaped as a function of the applied pressure, which can be probed experimentally. Theoretically, we find a peak for crystallization around 1.5 GPa relative to the experimental optimal pressure of 1.33 GPa for the observation of the insulating states. Consequently, TBLG provides a new platform for the exploration of Wigner physics and its relationship with superconductivity.

* phys.bikash@gmail.com

† dimer@illinois.edu

Twisted bi-layer graphene (TBLG) is a true example of emergence. Electrons in single layers of graphene are free while those in the composite consisting of two layers twisted close to the magic angle such that the electronic bands are essentially flat have almost no kinetic energy, E_K . In such cases, the physics is dominated by the interactions, E_U , between the electrons. The quantity $\lambda_s = a/(2 \sin \theta/2)$ captures the relationship between the original lattice constant, $a = 2.46 \text{ \AA}$, and the twist angle θ . $A_s n_s = 4$ fixes the superlattice density, with 4 the maximum number of electrons that occupy the lowest two bands and $A_s = \sqrt{3}\lambda_s^2/2$, the supercell area. Consequently, it is convenient to define the index $\nu = n_e A_s$ which serves as the electron filling. The initial experiments [1, 2] in this regime showed that insulating states can arise for $\nu = \pm 2, 3$. Doping away from $\nu = -2$ resulted in superconductivity with a transition temperature of 1.5 K. Cao, et. al. as well others [1–6] attributed the insulating states at $\nu = \pm 2, 3$ to Mott physics. Within this paradigm, insulating behavior should exist whenever the band is partially filled. However, metallic not insulating behavior exists at $\nu = 1$ in the experiments of Cao. et al. [1, 2] thereby ruling out Mott physics as the efficient cause of the insulating states [7].

The new experiments [8] in which the hydrostatic pressure between the layers is the tuning parameter address the conundrum of the $\nu = 1$ state. As expected, the new experiments confirm the initial results of Cao, et al. [1, 2] that insulating states exist at $\nu = 2, 3$ with superconductivity lurking nearby. However, increasing the hydrostatic pressure to 1.33 GPa destroys the metallic state at $\nu = 1$ giving rise to an insulator. In fact, hydrostatic pressure enhances the insulating state at all the other commensurate fillings. They also concluded [8] that the $\nu = 1$ state is spin-polarized as is $\nu = 3$, while that at $\nu = 2$ is a singlet, further evidence that Mottness is irrelevant to TBLG as it cannot explain the spin dependence of the insulating states.

This paper addresses the pressure dependence of the insulating states. Electronic band structure calculations [9–11] as a function of pressure in TBLG offer immediate insight into the physics at play. As expected, hydrostatic pressure increases the interlayer tunneling, thereby changing the magic angle condition. However, an additional feature also appears: the bandwidth shows a dome-like shape with increasing pressure. Because the interactions remain fixed, the ratio $r_s = E_U/E_K$ increases. In 2D, with one-electron per unit cell, exceeding the threshold $r_s > 37$ [12] results in Wigner crystallization (WC) on a triangular lattice. The question arises: Does increasing the pressure in TBLG lead to $r_s > 37$, thereby

resolving the pressure-induced metal-insulator transition in TBLG. We map out the phase diagram here using realistic parameters for TBLG and determine the regime where the $\nu = 1$ state crosses the WC threshold. We find that the new experiments at 1.33 GPa and 2.21 GPa are well within the Wigner regime while those at ambient pressure correspond to $r_s \ll 37$. Hence, the pressure-dependent data offers a clear confirmation of the WC proposal for the origin of the insulating states in TBLG. We also confirm the experimental trend that hydrostatic pressure enhances the insulating states (proposed[7] here to be a hierarchy of Wigner crystals on honeycomb and kagome lattices) at $\nu = 2, 3$.

We start by computing the pressure-dependent band structure and subsequently r_s . In our discussion, we will focus explicitly on device D2 of [8]. Consider two layers of graphene, each rotated by $\pm\theta/2$ around an axis passing through an A_1B_2 site, where the subscripts denote the layers, and A, B are sublattice labels. When θ is small, the supercell consists of a large number of atoms $\sim 10^4$, making *ab initio* methods [13] less viable or reliable [14] than the tight-binding schemes [15, 16]. Here we follow the tight-binding scheme of [9] where the tight-binding parameters are functions of pressure. Also, since we work with a tight-binding model, unlike the case of a continuum model, we limit our discussion to commensurate structures which obtain [17] for twist angles,

$$\theta = \cos^{-1} \left[\frac{m^2 + 4mn + n^2}{2(m^2 + mn + n^2)} \right], \quad m, n \in \mathbb{Z}. \quad (1)$$

The twist angle of the D2 sample is $\theta = 1.27^\circ$, which is not a commensurate angle. Because of the reasoning above, we work with the nearest commensurate angle, $\theta \approx 1.25^\circ$, obtained for $(m, n) = (26, 27)$. Here the supercell vectors are $\mathbf{R}_1 = m\mathbf{a}_1 + n\mathbf{a}_2$ and $\mathbf{R}_2 = -n\mathbf{a}_1 + (m+n)\mathbf{a}_2$ and each unit cell is $|m - n|$ ($= 1$ for D2) times larger than the moiré periodicity, λ_s . For commensurate structures, there is a well defined moiré Brillouin zone (MBZ). The symmetry points of the MBZ will be labeled as $\bar{\Gamma}$ (zone center), \bar{M} (edge center), and \bar{K} (zone corner). Since tunneling between two valleys is prevented in a low-energy description ($\lesssim 1$ eV) and as a result of the valley degeneracy, our calculation only considers an MBZ formed near the \mathbf{K} (Dirac) point of the original lattice.

We begin with a simplified description, ignoring any angular dependence of the hybridization or the orbital overlaps. The generic non-interacting part of the Hamiltonian is

$$H = - \sum_{i,j} t(\mathbf{R}_i - \mathbf{R}_j) |\mathbf{R}_i\rangle \langle \mathbf{R}_j| + \text{H.c.}, \quad (2)$$

where $\mathbf{R}_i = \sum_{x,y,z} R_i^a \mathbf{e}_a$ is the atomic coordinate in the basis of $\{\mathbf{e}_a\}$, $|\mathbf{R}_i\rangle$ is the wave function at site i and the tunneling strength between sites i and j is measured by the tight-binding parameter $t(\mathbf{R}_i - \mathbf{R}_j)$. A first-principle derivation of this parameter is discussed in the App. A, which can be approximated as

$$t(r) \approx t_{\perp} \left(1 - \frac{r^2}{d_{\perp}^2} \right) \exp \left(-\frac{r^2}{2r_0 d_{\perp}} \right). \quad (3)$$

Here $r_0 = 0.318 a_0$ is an isotropic decay length [14]. We use d_{\perp} for the inter-layer spacing at finite pressure P GPa and $d_{\perp}^0 = 3.35 \text{ \AA}$ is the spacing at ambient pressure. t_{\perp} is the σ -bond (or interlayer coupling) strength between the sp_2 orbitals of the AB stacked bilayers at some pressure P GPa. At ambient pressure $t_{\perp}|_{P=0} \equiv t_{\perp}^0 \approx 0.31 \text{ eV}$. Note that, in our discussion, t_{\perp} is the only natural parameter which is affected by pressure [see Eq. (6)]. The in-plane quantities such as lattice constant or in-plane hopping may change under very high pressure, especially in the presence of a hBN substrate; however, for the range of pressure relevant here, such effects can be safely neglected [9].

In order to quantify the effect of pressure on t_{\perp} , we first need to relate d_{\perp} to the pressure. Application of hydrostatic pressure along the c-axis can readily reduce d_{\perp} , the experimental consequences of which have been studied in [8]. This compression factor, denoted by δ_d , is related to applied pressure through the Murnaghan equation of state [11]

$$1 - \frac{d_{\perp}}{d_{\perp}^0} \equiv \delta_d = 10.48 \log \left(1 + \frac{P}{5.73} \right) \%. \quad (4)$$

The numbers appearing here are fixed using density functional theory [9]. An immediate consequence of a reduced d_{\perp} is an enhanced magic angle, which we denote by $\theta_{\text{magic}}^{\text{eff}}$. In fact, for experimentally accessible pressures, this mechanism can enhance $\theta_{\text{magic}}^{\text{eff}}$ up to 3° . The primary advantage of a large $\theta_{\text{magic}}^{\text{eff}}$ is an enhanced Coulomb energy scale ($E_U \sim \lambda_{\theta}^{-1} \sim \theta$) which could also result in an increased T_c [8].

In order to express t_{\perp} as a function of δ_d (hence, P), we use methods developed in [9–11]. At finite pressure the overlap between the Wannier orbitals develops a strong angular dependency (owing to triangular warping of the p_z orbitals) which is captured by a 10-parameter (in the δ_d – space) model

$$t_{\perp}(\mathbf{r}) = V_0(r) + V_3(r) [\cos(3\theta_{12}) + \cos(3\theta_{21})] + V_6(r) [\cos(6\theta_{12}) + \cos(6\theta_{21})], \quad (5)$$

where θ_{ij} are the angles between the vectors connecting i^{th} -site to j^{th} -site and that connecting i^{th} site to its nearest-neighbor. The radial overlap functions, $V_{|m|}(r)$, are measures

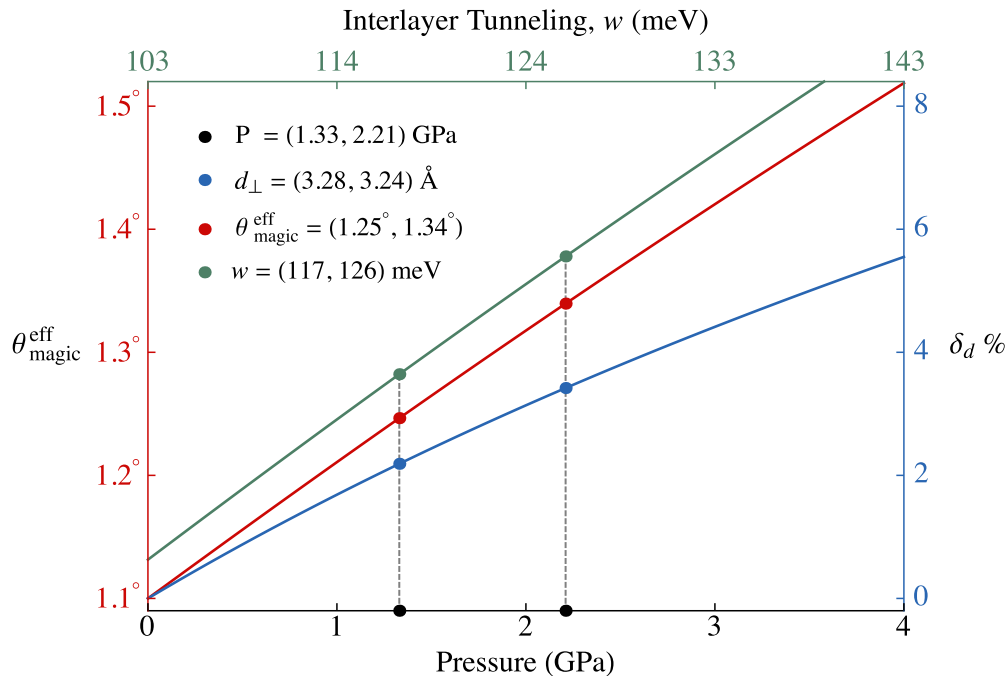


FIG. 1. With increasing external pressure, the inter-layer distance decreases by $\delta_d\%$ (blue curve or right axis) which is described in Eq. (4). Reduced separation enhances inter-layer tunneling, $w \approx t_{\perp}/3$ (green curve or top axis), as can be seen from Eq. (6). This causes an increase (red curve or left axis) in the effective magic angle, $\theta_{\text{magic}}^{\text{eff}}$, where the band become the flattest, see Eq. (7). The dots correspond to the reported values of pressure where the measurements of [8] were performed.

of the hybridization between Wannier orbitals with $m = 0, \pm 3, \pm 6$ angular momenta. We write out their exact functional forms in the App. B as well as the numerical values of the 10 parameters required to fix these functions. For numerical accuracy, our computations are based on this model; however, for simplicity, from now onward, we confine our discussion only to the $m = 0$ component (p_z orbital), which is the most dominant contribution. In fact, as can be seen in App. A, it is $t_{\perp}(0)$ that roughly sets the scale for the interlayer tunneling. Consequently, we are down to just a one-parameter expression for $t_{\perp}(\mathbf{r})$

$$t_{\perp}(\delta_d) = t_{\perp}^{(0)} - t_{\perp}^{(1)}\delta_d + t_{\perp}^{(2)}\delta_d^2 \quad , \quad t_{\perp}^{(0,1,2)} \simeq (0.31, -1.73, 7.12) \text{ eV} . \quad (6)$$

The parameters $t_{\perp}^{(i)}$ s above, which marginally differ from those listed in the App. B, can be seen as effective leading parameters after incorporating the angular contributions.

Using Eq. (6), we now obtain the pressure dependence of $\theta_{\text{magic}}^{\text{eff}}$ discussed before. Note

that the magic angle is (roughly) obtained by matching the quasiparticle kinetic energy, $\hbar v_0 K_\theta$, and the hybridization scale, t_\perp . Here $v_0 = 10^6$ m/s is the speed of the electrons in pristine graphene and $K_\theta = 4\pi/3\lambda_s$ is the size of the MBZ. This causes $\theta_{\text{magic}}^{\text{eff}} \sim t_\perp$, or at ambient pressure, $\theta_{\text{magic}} \sim t_\perp^{(0)}$. Thus, $\hbar v_0 K_\theta = \theta_{\text{magic}}^{\text{eff}} (2t_\perp^{(0)}/\theta_{\text{magic}})$. Following [8, 9, 11], we set $\theta_{\text{magic}} = 1.1^\circ$. This gives rise to the following expression for the effective magic angle

$$\frac{\theta_{\text{magic}}^{\text{eff}}(\text{P})}{\theta_{\text{magic}}} = \frac{t_\perp(\text{P})}{t_\perp^0} = 1 + 5.584 \delta_d + 22.97 \delta_d^2. \quad (7)$$

Fig. 1 displays the relevant parameters discussed above as functions of external pressure. For a given device with a fixed twist angle θ , which is larger than the ambient pressure magic angle θ_{magic} , as pressure increases one gradually increases $\theta_{\text{magic}}^{\text{eff}}$. For $\theta = \theta_{\text{magic}}^{\text{eff}}$, one defines the optimum pressure for a particular system, P_{opt} , which is also coincident with the flat-band condition. Increasing the pressure further will relatively tune the system away from the magic angle. The optimal pressure for device D2, for instance, can be solved by demanding $\theta_{\text{magic}}^{\text{eff}} = 1.27^\circ$. From Eq. (7), we find that $\text{P} \simeq 1.55$ GPa ($\delta_d = 2.5\%$). This explains why optimal behavior is seen (among the two available data sets) around 1.33 GPa ($\delta_d = 2.2\%$), as opposed to near 2.21 GPa ($\delta_d = 3.4\%$).

With the use of these parameters, we compute the band structure. The most notable feature in Fig. 2 is that the bandwidth shrinks as 1.33 GPa is approached and increases beyond this pressure. It is this feature that gives rise to the dome-like shape of the phase diagram of r_s versus hydrostatic pressure, thereby affecting the observed insulating behavior. Note that, although here we used the tight-binding description, one may also use the effective low energy descriptions developed for ambient pressure [5, 18–21]; albeit the (tight-binding or continuum) parameters must be fixed taking finite pressure into account.

We now turn to the computation of r_s . We need first the Coulomb energy for a TBLG system at θ angle, $E_U = (\alpha/\epsilon) (\hbar v_0/a) (a/r_e)$. Since v_0 is about 300 times smaller than the speed of light, the effective fine structure constant of (suspended) graphene is $\alpha \approx 2.2$. Also note that $\hbar v_0/a = 2.135$ eV. In the presence of the hBN substrate, this is reduced by a factor of the effective dielectric constant, $\epsilon = 10$ (see [7] for a justification of this value). The average inter-particle distance can be obtained from $\pi r_e^2 n_e = 1$. For a given filling fraction, $r_e = \sqrt{S_\theta/\pi\nu} \approx 0.525 \lambda_s/\sqrt{\nu}$. Combining all of these expressions, we find that

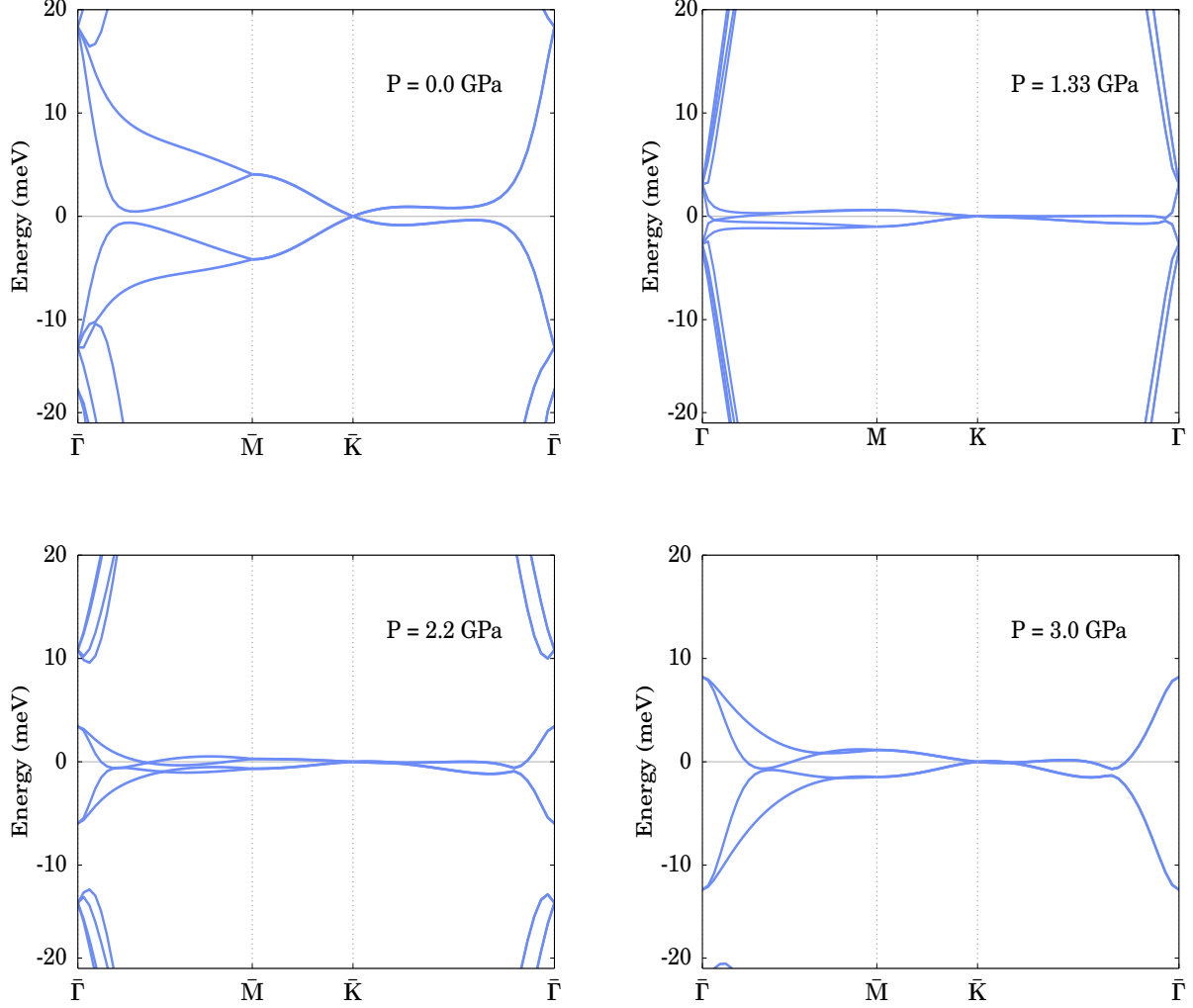


FIG. 2. Pressure-dependent band dispersion of TBLG for $\theta = 1.25^\circ$. The parameters used in obtaining these are listed in the App. B. With increasing pressure, the low energy bands become flatter; however, beyond $\sim 1.45 \pm 0.1$ GPa, the bandwidth increases subsequently. The reason behind such an optimal behavior can be understood from Eq. (7).

$E_U \approx (15 \text{ meV}) \theta^\circ$. The resultant expression for r_s is

$$r_s \approx 15 \text{ meV} \frac{\theta^\circ}{E_K} \sqrt{\nu} \xrightarrow{\text{Device D2}} \frac{20 \text{ meV}}{E_K \text{ meV}} \sqrt{\nu}. \quad (8)$$

In order to fix the kinetic energy above, we first relate the carrier concentration to chemical potential, μ , and since $E_K \lesssim \mu$, for a minimal (and hence conservative) estimate of r_s , one can substitute E_K with μ . This is discussed in detail in App. C. In Fig. 3 we plot the behavior of r_s as a function of pressure, which is clearly dome-like. The key aspect of this figure is

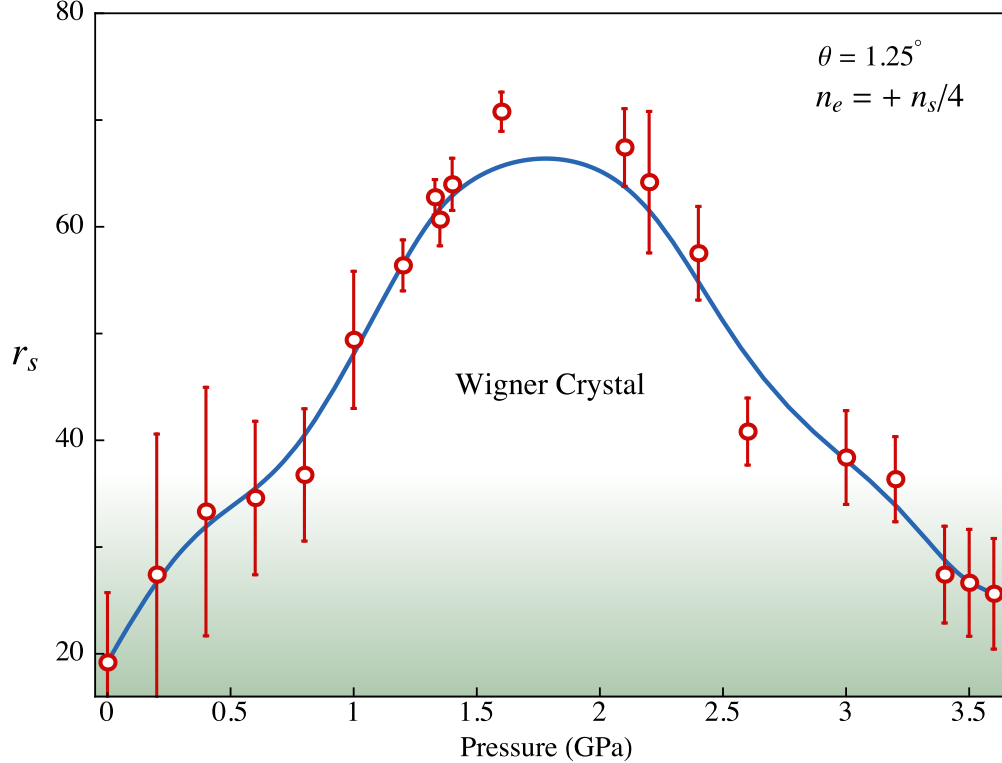


FIG. 3. For the device D2 of [8], we compute r_s (red dots along with computational error associated with coarse graining of the k -space) of the quarter-filling state. The blue curve provides a guide for the eye. Its dome-like behavior can explain a similar feature seen in the conductance of the quarter-filling state in the experiment of [8]. For the pressure window of $\sim 1 - 3$ GPa the system enters Wigner crystallization regime, $r_s \gtrsim 37$. Similar behavior is obtained for $n_e = n_s/2$ and $3n_s/4$.

the crossing of the Wigner threshold for pressures in the range $0.75 \text{ GPa} < P < 3 \text{ GPa}$. The existence of this window for optimal insulating behavior of the $\nu = 1$ state can be tested experimentally. We find that $P_{\text{opt}} = 1.5 \text{ GPa}$ which is close to the experimentally observed optimal pressure, 1.33 GPa . Clearly further experiments are needed to map out the non-monotonic dependence of the metal-insulator transition as a function of the hydrostatic pressure. As we discuss in App. C, similar behavior is seen for the $\nu = 2, 3$ states, which as we showed previously [7] correspond to honeycomb and kagome Wigner crystals.

We have shown that the pressure dependence of the metal-insulator transition has a natural explanation within the hierarchy of Wigner crystals proposed recently for TBLG [7]. Regarding the spin dependence of the insulating states, the ferromagnetic triangular WC is

well known [12] to be energetically favored as in the $\nu = 1$ experiments. The hexagonal WC we proposed has explicitly two electrons residing in each moiré cell and hence has $S = 0$. The spin structure of the kagome lattice has no natural singlet correlations and hence should be spin-polarized just as in the $\nu = 1$ case. Consequently, all the features of the novel insulating states in TBLG are captured by a transition to WC. Should the dome-like phase diagram for the $\nu = 1$ state be confirmed experimentally, then this would add significant substantiation to the claim that TBLG offers a playground for observing Wigner crystallization and the possible onset of superconductivity.

Acknowledgement: BP is thnakful to Yubo Yang for his generous help with the numerics. We are thankful to Chandan Setty for his characteristically level-headed remarks and the NSF DMR-1461952 for partial funding of this project.

Appendix A: Tight-binding Approximation

Considering a simple linear combination of p_z orbitals, one can express the tight-binding parameter in Eq. (2) as

$$t(\mathbf{R}) = V_{pp\pi}(\mathbf{R}) \sin^2 \gamma + V_{pp\sigma}(\mathbf{R}) \cos^2 \gamma \quad , \quad R \cos \gamma = \mathbf{R} \cdot \mathbf{e}_z . \quad (\text{A1})$$

Here R is the length of the vector \mathbf{R} joining two atoms and the overlap or transfer integrals are expressed in terms of the Slater-Koster parameters [22]

$$V_{pp\pi}(\mathbf{R}) = -t_0 \exp\left(-\frac{R - a_0}{r_0}\right) \quad , \quad V_{pp\sigma}(\mathbf{R}) = t_{\perp} \exp\left(-\frac{R - d_{\perp}}{r_0}\right) . \quad (\text{A2})$$

$r_0 = 0.318 a_0$ is an isotropic decay length chosen [14] for the transfer integrals so that the next-nearest in-plane overlap becomes [23] $0.1t_0$. $t_0 \approx 2.7$ eV is the in-plane π -bond strength of the two neighboring p_z orbitals (separated by $a_0 = a/\sqrt{3} = 1.42$ Å) in single-layer graphene.

Since $d_{\perp}/a_0 \gtrsim 2$, near the stacking center, the tunneling parameter $t(\mathbf{R})$ is largely dominated by the σ -bond, and thus, the function $t(\mathbf{R})$ can be approximated as

$$t(r) \approx t_{\perp} \left(1 - \frac{r^2}{d_{\perp}^2}\right) \exp\left(-\frac{r^2}{2r_0 d_{\perp}}\right) . \quad (\text{A3})$$

In the inset of Fig. A1, the behavior of Eq. (A3) is juxtaposed with the exact result from Eq. (A1), which shows an exponential reduction of the tunneling strength for $r \gtrsim d_{\perp}$. This also causes the Fourier transform to sharply decay for any $k \gtrsim 1/d_{\perp}$. Thus, for a low-energy model, it is sufficient to work with $t_{\perp}(\mathbf{K})$ only and not include the higher modes, such as $t_{\perp}(\mathbf{K} + \mathbf{G})$, where \mathbf{G} is a moiré reciprocal lattice vector. One can perform a Fourier transform of $t(\mathbf{r})$ computed above to determine $t_{\perp}(\mathbf{K})$, or since we work in the $\theta \rightarrow 0$ limit (for AB stacking), one can approximate $t_{\perp}(\mathbf{K})/A_0 \equiv w = \frac{1}{3}t_{\perp}$. Here $A_0 = \sqrt{3}a^2/2$ is the area of the single-layer graphene unit cell and 3 appears to take into account that there are three equivalent Dirac cones. One can use w as the input parameter in the effective theories.

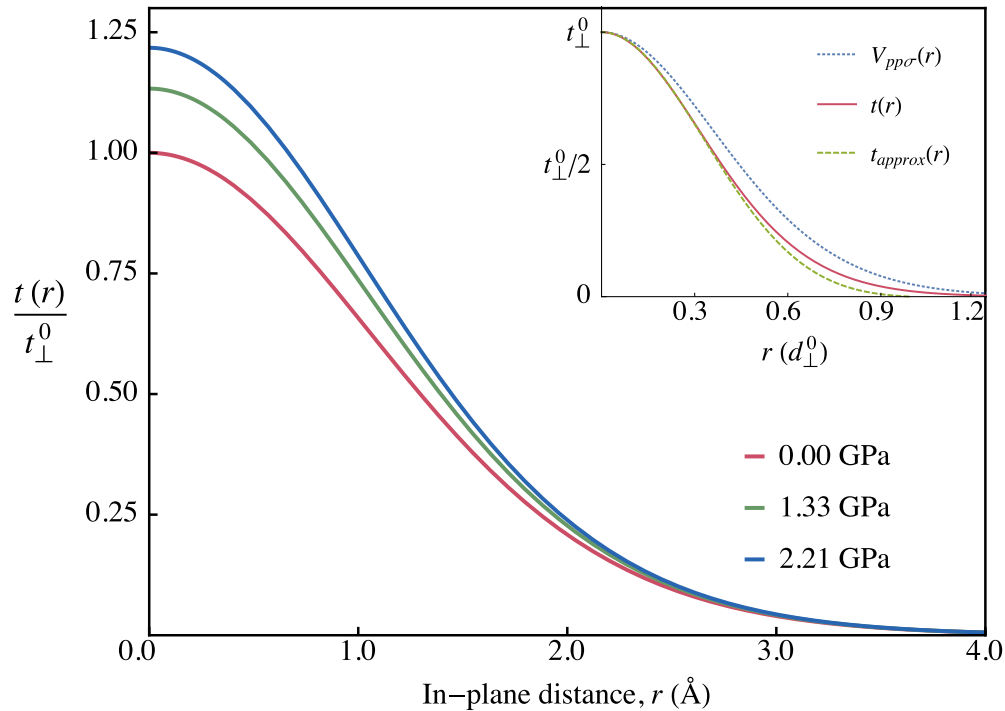


FIG. A1. Inter-layer tunneling for different pressures as a function of distance from the site of rotation. With increasing pressure, the inter-layer distance decreases causing the tunneling strength to increase. (Inset) The dominant contribution to $t(r)$ comes from $V_{pp\sigma}$ which leads to a simpler expression in Eq. (A3).

Appendix B: Overlap Functions of Wannier Orbitals

The radial functions described in Eq. (5) are

$$V_0(r) = \lambda_0 e^{-\xi_0 \bar{r}^2} \cos(\kappa_0 \bar{r}), \quad (\text{A1a})$$

$$V_3(r) = \lambda_3 \bar{r}^2 e^{-\xi_3 (\bar{r} - x_3)^2}, \quad (\text{A1b})$$

$$V_6(r) = \lambda_6 e^{-\xi_6 (\bar{r} - x_6)^2} \sin(\kappa_6 \bar{r}). \quad (\text{A1c})$$

Here $\bar{r} = r/a$. The strongest contributions to inter-layer tunneling come from the hybridization scales λ_i s. The remaining parameters, the length scales associated with the Wannier orbitals, remain weakly dependent on pressure. All the parameters appearing above, collectively denoted by $\pi_i(\delta_d)$ where $i = 1, 2, \dots, 10$, are fixed [9] using conventional density functional methods and are listed in the Table A1. Given the pressure range of interest, the functional dependence of $\pi_i(\delta_d)$ with δ_d is truncated given by a quadratic fit

$$\pi_i(\delta_d) = c_i^{(0)} - c_i^{(1)} \delta_d + c_i^{(2)} \delta_d^2. \quad (\text{A2})$$

TABLE A1. Compression, δ_d , dependence of the 10 parameters appearing in Eq. (A1). The coefficients, $c_i^{(n)}$, appearing in Eq. (A2) are listed below (in eV units). This table first appeared in Ref. [9].

| i (π_i) | $c_i^{(0)}$ | $c_i^{(1)}$ | $c_i^{(2)}$ |
|-------------------|-------------|-------------|-------------|
| 1 (λ_0) | 0.310 | -1.882 | 7.741 |
| 2 (ξ_0) | 1.750 | -1.618 | 1.848 |
| 3 (κ_0) | 1.990 | 1.007 | 2.427 |
| 4 (λ_3) | -0.068 | 0.399 | -1.739 |
| 5 (ξ_3) | 3.286 | -0.914 | 12.011 |
| 6 (x_3) | 0.500 | 0.322 | 0.908 |
| 7 (λ_6) | -0.008 | 0.046 | -0.183 |
| 8 (ξ_6) | 2.272 | -0.721 | -4.414 |
| 9 (x_6) | 1.217 | 0.027 | -0.658 |
| 10 (κ_6) | 1.562 | -0.371 | -0.134 |

Appendix C: Method of Computing r_s

Here we discuss how E_K appearing in Eq. (8) is fixed from the band structure. We first compute the density of states (DOS), $n(\epsilon)$, which can be normalized in the following way. Since each moiré supercell contains 8 electrons at the most, integrating the DOS for the bottom four bands must yield 8

$$\int_{\Lambda_h}^{\Lambda_e} n(\epsilon) d\epsilon = 8. \quad (\text{A1})$$

Here $\Lambda_{e,h} \sim 10$ meV, respectively, provide the upper and lower cut-off for the bottom 4 bands. Integrating the normalized DOS up to the chemical potential provides the carrier concentration (in interest of [8] we do so for the hole side)

$$n_e(\mu) = \int_{\Lambda_h}^{\mu} n(\epsilon) d\epsilon. \quad (\text{A2})$$

This is shown in Fig. A2a. In obtaining r_s for the $\nu/4$ state one can fix $n_e(\mu) = \nu n_s/4$ (e.g., see the gray line for $\nu = 1$) and obtain how μ evolves with pressure along that line. This is the procedure we used for E_K . Fig. A2b shows r_s as a function of pressure for $\nu = 2, 3$ states. Note the source of error here is the coarse graining of the energy integral above.

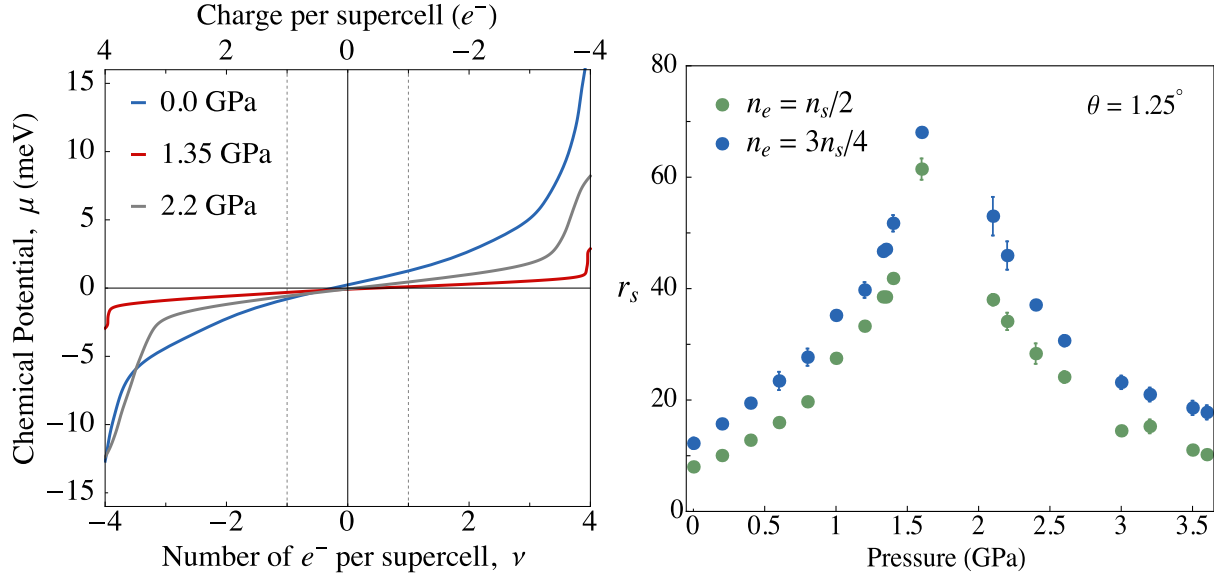


FIG. A2. (Left) The chemical potential dependence (smoothly fitted) of the carrier concentration for various pressures, as obtained in Eq. (A2). (Right) r_s as a function of pressure obtained for $\nu = 2, 3$ states. Similar to the $\nu = 1$ state discussed in the main text they also exhibit dome-like behavior.

-
- [1] Yuan Cao, Valla Fatemi, Ahmet Demir, Shiang Fang, Spencer L Tomarken, Jason Y Luo, Javier D Sanchez-Yamagishi, Kenji Watanabe, Takashi Taniguchi, Efthimios Kaxiras, Ray C. Ashoori, and Pablo Jarillo-Herrero, “Correlated insulator behaviour at half-filling in magic-angle graphene superlattices,” *Nature* **556**, 80 (2018).
- [2] Yuan Cao, Valla Fatemi, Shiang Fang, Kenji Watanabe, Takashi Taniguchi, Efthimios Kaxiras, and Pablo Jarillo-Herrero, “Unconventional superconductivity in magic-angle graphene superlattices,” *Nature* **556**, 43 (2018).
- [3] Cenke Xu and Leon Balents, “Topological superconductivity in twisted multilayer graphene,” *Phys. Rev. Lett.* **121**, 087001 (2018).
- [4] L. Zou, H. C. Po, A. Vishwanath, and T. Senthil, “Band Structure of Twisted Bilayer Graphene: Emergent Symmetries, Commensurate Approximants and Wannier Obstructions,” ArXiv e-prints (2018), [arXiv:1806.07873 \[cond-mat.str-el\]](https://arxiv.org/abs/1806.07873).
- [5] Noah F. Q. Yuan and Liang Fu, “Model for the metal-insulator transition in graphene superlattices and beyond,” *Phys. Rev. B* **98**, 045103 (2018).
- [6] Ganapathy Baskaran, “Theory of emergent josephson lattice in neutral twisted bilayer graphene (moiré is different),” [arXiv:1804.00627](https://arxiv.org/abs/1804.00627) (2018).
- [7] Bikash Padhi, Chandan Setty, and Philip Phillips, “Doped twisted bilayer graphene near magic angles: Proximity to wigner crystallization not mott insulation,” *Nano Letters* (2018).
- [8] Matthew Yankowitz, Shaowen Chen, Hryhoriy Polshyn, K Watanabe, T Taniguchi, David Graf, Andrea F Young, and Cory R Dean, “Tuning superconductivity in twisted bilayer graphene,” [arXiv preprint arXiv:1808.07865](https://arxiv.org/abs/1808.07865) (2018).
- [9] Stephen Carr, Shiang Fang, Pablo Jarillo-Herrero, and Efthimios Kaxiras, “Pressure dependence of the magic twist angle in graphene superlattices,” *Phys. Rev. B* **98**, 085144 (2018).
- [10] Shiang Fang and Efthimios Kaxiras, “Electronic structure theory of weakly interacting bilayers,” *Phys. Rev. B* **93**, 235153 (2016).
- [11] B. Lingam Chittari, N. Leconte, S. Javvaji, and J. Jung, “Pressure Induced Compression of Flatbands in Twisted Bilayer Graphene,” ArXiv e-prints (2018), [arXiv:1808.00104 \[cond-mat.mes-hall\]](https://arxiv.org/abs/1808.00104).

- [12] B. Tanatar and D. M. Ceperley, “Ground state of the two-dimensional electron gas,” *Phys. Rev. B* **39**, 5005–5016 (1989).
- [13] S. Shallcross, S. Sharma, and O. A. Pankratov, “Quantum interference at the twist boundary in graphene,” *Phys. Rev. Lett.* **101**, 056803 (2008).
- [14] G. Trambly de Laissardière, D. Mayou, and L. Magaud, “Localization of dirac electrons in rotated graphene bilayers,” *Nano Letters* **10**, 804–808 (2010).
- [15] J. M. B. Lopes dos Santos, N. M. R. Peres, and A. H. Castro Neto, “Graphene bilayer with a twist: Electronic structure,” *Phys. Rev. Lett.* **99**, 256802 (2007).
- [16] J. M. B. Lopes dos Santos, N. M. R. Peres, and A. H. Castro Neto, “Continuum model of the twisted graphene bilayer,” *Phys. Rev. B* **86**, 155449 (2012).
- [17] S. Shallcross, S. Sharma, E. Kandelaki, and O. A. Pankratov, “Electronic structure of turbostratic graphene,” *Phys. Rev. B* **81**, 165105 (2010).
- [18] Rafi Bistritzer and Allan H. MacDonald, “Moiré bands in twisted double-layer graphene,” *Proceedings of the National Academy of Sciences* **108**, 12233–12237 (2011).
- [19] M. Koshino, N. F. Q. Yuan, T. Koretsune, M. Ochi, K. Kuroki, and L. Fu, “Maximally-localized Wannier orbitals and the extended Hubbard model for the twisted bilayer graphene,” ArXiv e-prints (2018), [arXiv:1805.06819](https://arxiv.org/abs/1805.06819) [cond-mat.mes-hall].
- [20] H. C. Po, L. Zou, A. Vishwanath, and T. Senthil, “Origin of Mott insulating behavior and superconductivity in twisted bilayer graphene,” ArXiv e-prints (2018), [arXiv:1803.09742](https://arxiv.org/abs/1803.09742) [cond-mat.str-el].
- [21] H. C. Po, L. Zou, T. Senthil, and A. Vishwanath, “Faithful Tight-binding Models and Fragile Topology of Magic-angle Bilayer Graphene,” ArXiv e-prints (2018), [arXiv:1808.02482](https://arxiv.org/abs/1808.02482) [cond-mat.str-el].
- [22] J. C. Slater and G. F. Koster, “Simplified lcao method for the periodic potential problem,” *Phys. Rev.* **94**, 1498–1524 (1954).
- [23] R. S. Deacon, K.-C. Chuang, R. J. Nicholas, K. S. Novoselov, and A. K. Geim, “Cyclotron resonance study of the electron and hole velocity in graphene monolayers,” *Phys. Rev. B* **76**, 081406 (2007).